

ADVANCED MATERIALS

Supporting Information

for *Adv. Mater.*, DOI: 10.1002/adma.202110664

Topological Crystalline Insulator Candidate ErAsS with
Hourglass Fermion and Magnetic-Tuned Topological
Phase Transition

*Hongxiang Chen, Jiacheng Gao, Long Chen, Gang
Wang,* Hang Li, Yulong Wang, Juanjuan Liu, Jinchen
Wang, Daiyu Geng, Qinghua Zhang, Jieming Sheng,
Feng Ye, Tian Qian, Lan Chen, Hongming Weng,* Jie
Ma,* and Xiaolong Chen**

Supporting Information

Topological crystalline insulator candidate ErAsS with hourglass fermion and magnetic-tuned topological phase transition

Hongxiang Chen, Jiacheng Gao, Long Chen, Gang Wang*, Hang Li, Yulong Wang, Juanjuan Liu, Jinchun Wang, Daiyu Geng, Qinghua Zhang, Jieming Sheng, Feng Ye, Tian Qian, Lan Chen, Hongming Weng*, Jie Ma*, Xiaolong Chen*

1. Crystal structure

1.1 X-ray diffraction (XRD)

XRD pattern of an as-grown ErAsS single crystal (Fig. S1) was collected using a PANalytical X'Pert PRO diffractometer (Cu K_{α} radiation, $\lambda = 1.54178 \text{ \AA}$) operated at 40 kV and 40 mA with a graphite monochromator in the reflection mode ($2\theta = 5^{\circ}$ – 100° ; step = 0.017°). The diffraction peaks were collected on the large plane, giving an inter-plane distance about 16.5 \AA .

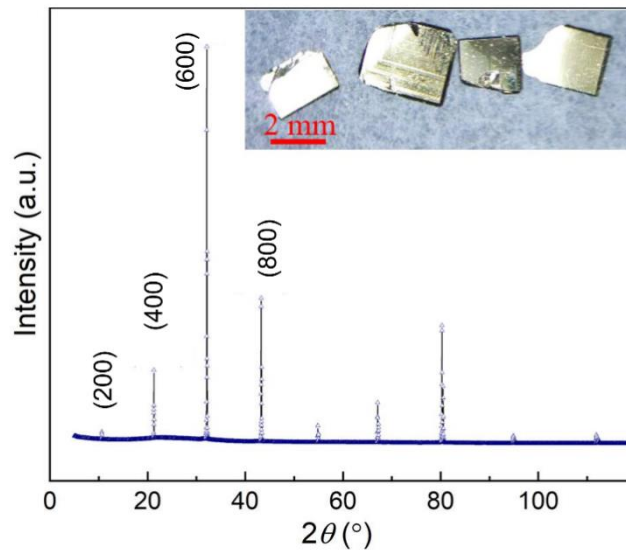


Figure S1. The XRD pattern of ErAsS single crystal, showing $(h00)$ ($h = \text{even number}$) diffraction peaks. The inset shows the optical photograph of ErAsS single crystals.

To further determine the crystal structure of ErAsS, intensity data of an as-grown single crystal were collected at 297 K. The raw data were processed by the SAINT program, and absorption

corrections were made by using the multi-scans method. The structural model of ErAsS in *Pnma* was initiated by the direct method and refined by the full-matrix least-squares methods using the SHELXTL software package [1] and OLEX2 [2]. The corresponding crystallographic data, atomic coordinates, and equivalent isotropic displacement parameters are shown in Table S1 and S2, respectively. The lattice parameter *a* refined from single crystal data is consistent with that of the XRD indexing result.

Table S1. Crystallographic data from the Rietveld refinement for ErAsS.

Empirical formula	ErAsS
CCDC number	2128765
Formula weight	274.24 g/mol
Space group / Z	<i>Pnma</i> (No. 62) /4
Unit cell dimensions	$a = 16.7493(12) \text{ \AA}$ $\alpha = 90^\circ$ $b = 3.7782(2) \text{ \AA}$ $\beta = 90^\circ$ $c = 3.8087(2) \text{ \AA}$ $\gamma = 90^\circ$
Volume / d_{cal}	241.02(2) \AA^3 / 7.558 g/cm ³
Reflections collected/R(int)	2522 / 0.0785
Data / restraints / parameters	310 / 0 / 20
Goodness-of-fit on F^2	1.079
Final R indices [I > 2sigma(I)]	$R_1 = 0.0366$, $wR_2 = 0.1054$
R indices (all data)	$R_1 = 0.0369$, $wR_2 = 0.1057$
Largest diff. peak and hole	3.189 and -2.219 e. \AA^{-3}

Table S2. Atomic coordinates and equivalent isotropic displacement parameters for orthorhombic ErAsS.

Atom	Wyck.	Site symm.	<i>x/a</i>	<i>y/b</i>	<i>z/c</i>	$U(\text{eq})(\text{\AA}^2)$
Er	4 <i>c</i>	<i>m</i>	0.35449(3)	0.7500	0.23431(14)	0.0081(4)
As	4 <i>c</i>	<i>m</i>	0.49878(10)	0.7500	0.7205(3)	0.0086(5)
S	4 <i>c</i>	<i>m</i>	0.3135(2)	0.2500	0.7357(6)	0.0076(8)

1.2 Scanning transmission electron microscopy (STEM)

Standard focused ion beam (FIB) technique was used to prepare thin lamella for STEM. Cross-sectional lamella in *ac*- or *ab*-plane were thinned down to 100 nm at an accelerating voltage of 30 kV with a decreasing current from the maximum 2.5 nA, followed by fine polish at an accelerating voltage of 2 kV with a small current of 40 pA.

1.3 Chemical composition

The chemical composition of ErAsS single crystals with clean surface was determined by an inductively coupled plasma-atomic emission spectrometry (ICP-AES, Leeman Prodigy 7). The normalized Er : As : S ratio was 0.99(1) : 1.00(1) : 1.01(1).

2. Neutron diffraction

The magnetic structure of ground state ($T = 2.22$ K) was determined to have a type-IV magnetic space group (P_a2_1/m (No. 11.55)) with the refinement parameters $R_p = 4.7\%$ and $R_{wp} = 8.6\%$.

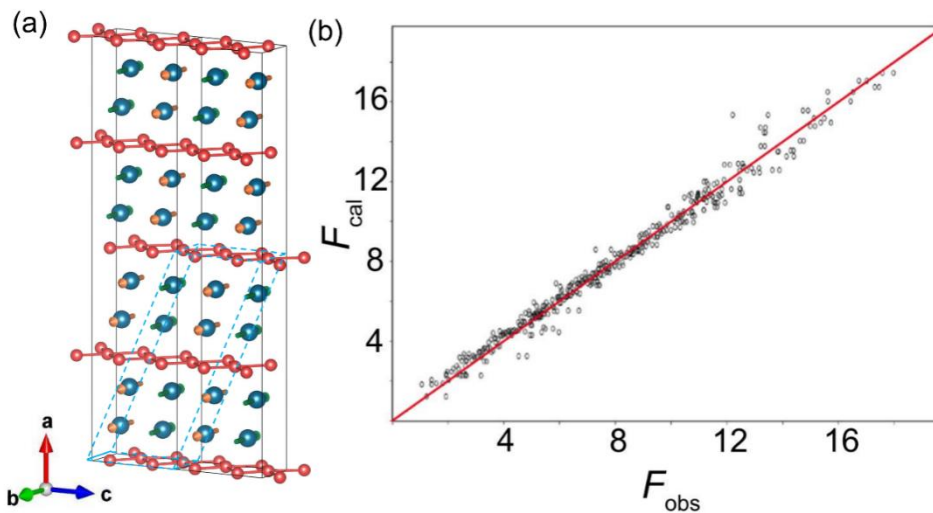


Figure S2. (a) The schematic magnetic structure of ErAsS at 2.22 K. The black cell is the magnetic unit cell. The blue one is the primitive cell of collinear antiferromagnetic (AFM) state.

Only Er and As atoms are shown for clarity. (b) Refinement result of the magnetic structure at 2.22 K. The red line is the linear fit of calculated vs. experimental results.

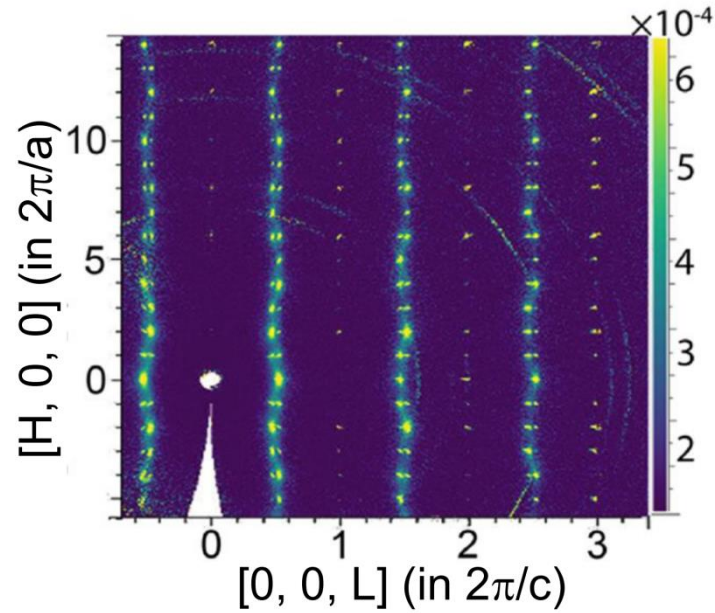


Figure S3. The contour plots of diffraction pattern in the reciprocal plane (H0L) at 3.5 K by subtracting the background of 10 K.

3. Magnetic susceptibility and specific heat capacity

Both magnetic susceptibility and heat capacity measurements revealed two magnetic states, as shown in Fig. S4. The transition temperatures in magnetic susceptibility are slightly different (~ 0.2 K) from those of specific heat capacity. The transition temperatures $T_N \sim 3.27$ K and $T_{ICM} \sim 3.65$ K from the heat capacity measurements were used in the manuscript.

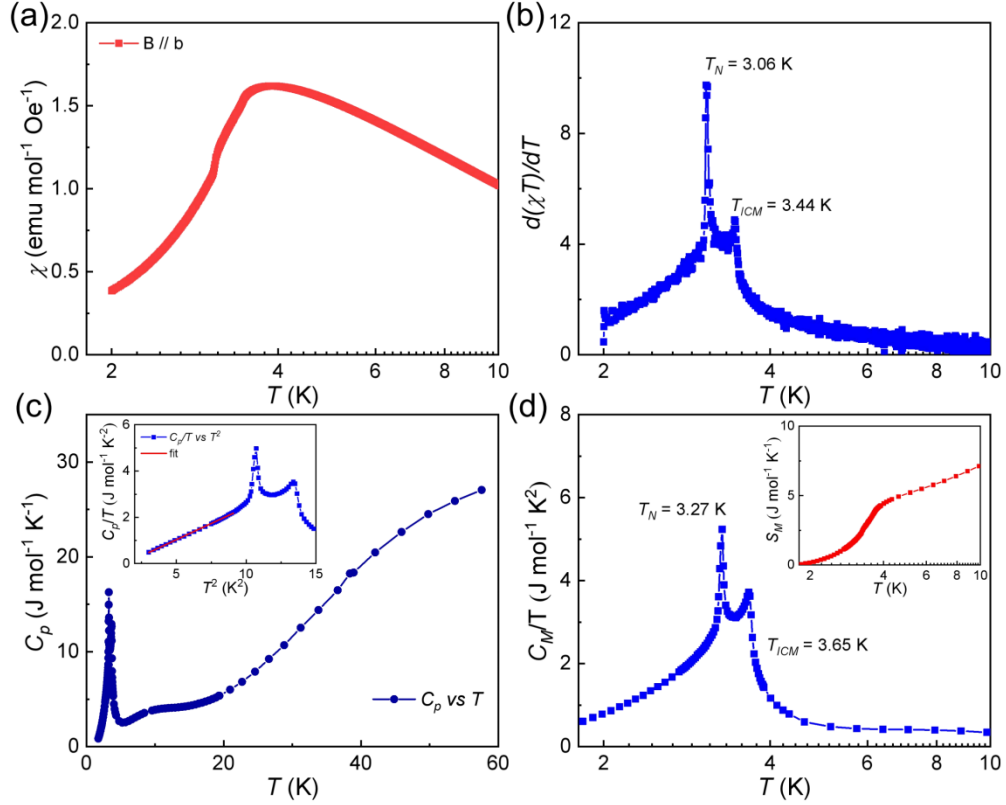


Figure S4. (a) The temperature dependence of magnetic susceptibility ($\chi - T$) with magnetic field parallel to the b axis and (b) the corresponding $d(\chi T)/dT$ curve. (c) The temperature dependence of specific heat capacity (C_p). The inset shows the fitting of $C_p/T = \beta + \gamma T^2$ from 1.7 K to 3.0 K. (d) The temperature dependence of C_M/T , where C_M represents the specific heat contribution of magnetism by subtracting the contribution of crystal lattice. The inset shows the corresponding magnetic entropy (S_M).

4. Calculated topological properties of ErAsS

4.1 Topological invariants of paramagnetic (PM) ErAsS

Table S3 shows the elementary layers in space group No. 62, from which we can see that the elementary layer L_1 is coincide with As-atom layer in ErAsS. Table S4 is all possible combination of above elementary layers. In our calculation, ErAsS belongs to the first line of Table S4, which means that its PM electronic structure can be understood by the stacking of L_1 .

Table S3. Topological invariants of elementary layer constructions of space group No. 62.

	Indicator	$m_{\frac{1}{2}0}^{010}$	$g_{\frac{111}{222}}^{100}$	$g_{\frac{1}{2}0\frac{1}{2}}^{001}$	i	$c_{\frac{1}{2}0}^{010}$	$c_{\frac{1}{2}0\frac{1}{2}}^{001}$	$c_{\frac{111}{222}}^{100}$
$L_1: (100; 0)$	(0002)	00	0	1	1	1	0	1
$L_2: (100; \frac{1}{4})$	(0000)	00	1	1	0	1	1	0
$L_3: (010; \frac{1}{4})$	(0000)	20	1	0	0	1	0	1

Table S4. Layer constructions with symmetry indicator (0002) of space group No. 62.

LC	$m_{\frac{1}{2}0}^{010}$	$g_{\frac{111}{222}}^{100}$	$g_{\frac{1}{2}0\frac{1}{2}}^{001}$	i	$c_{\frac{1}{2}0}^{010}$	$c_{\frac{1}{2}0\frac{1}{2}}^{001}$	$c_{\frac{111}{222}}^{100}$
L_1	00	0	1	1	1	0	1
$L_1 + L_2$	00	1	0	1	0	1	1
$L_1 + L_3$	20	0	1	1	0	0	0
$L_1 + L_2 + L_3$	20	0	0	1	1	1	0

4.2 Topological properties of PM ErAsS

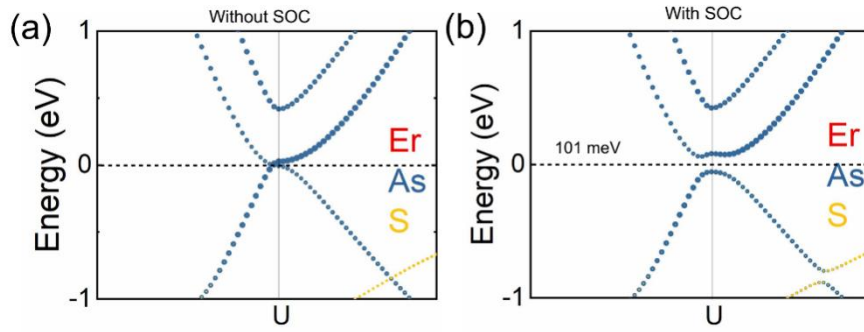


Figure S5. Zoomed band structure around high-symmetry point U without (a) and with (b) spin-orbit coupling.

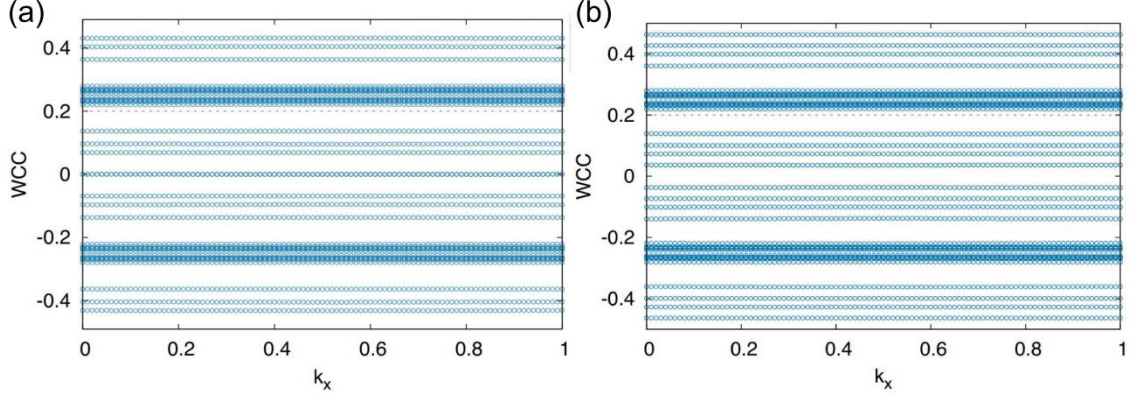


Figure S6. The Wilson loop spectra for subspace with $+i$ mirror eigenvalue on (a) $k_y = 0$ and (b) $k_y = \pi$ plane. The loop is defined as a reciprocal lattice vector along $[001]$. The red dotted lines are reference lines, from which we can see that the spectra have no crossing with reference lines.

The mirror Chern number in PM ErAsS is calculated to be zero, as shown in Fig. S6. On the two mirror invariant planes, the evolution of Wilson loop spectra for the subspace with $+i$ mirror eigenvalue is trivial.

The glide invariant can be calculated by the topological index χ [3, 4], and Alexandradinata, et al. provided a simple way to calculate the index [5], $\chi = 2\mathcal{S}_{\Gamma X}^+ + \mathcal{S}_{XM} + 2\mathcal{S}_{MY}^+$, where \mathcal{S}_{XM} is the sign of velocity at the crossing point between the reference line and the Wilson loop spectrum along $\tilde{X} - \tilde{M}$, the same as $\mathcal{S}_{\Gamma X}^+$ and \mathcal{S}_{MY}^+ , and the superscript means the $+i$ branch of Wilson loop spectrum. By choosing a reference line which only crosses the Wilson loop spectrum (Fig. 4b) along $\tilde{X} - \tilde{M}$ and $\tilde{Y} - \tilde{\Gamma}$, the Wilson loop spectrum along $\tilde{X} - \tilde{M}$ is two-fold degenerate ($\mathcal{S}_{XM} = 2$). Thus the topological index in ErAsS is calculated to be $\chi = 2$, corresponding to a nontrivial glide invariant.

4.3 Electronic structure of collinear AFM ErAsS

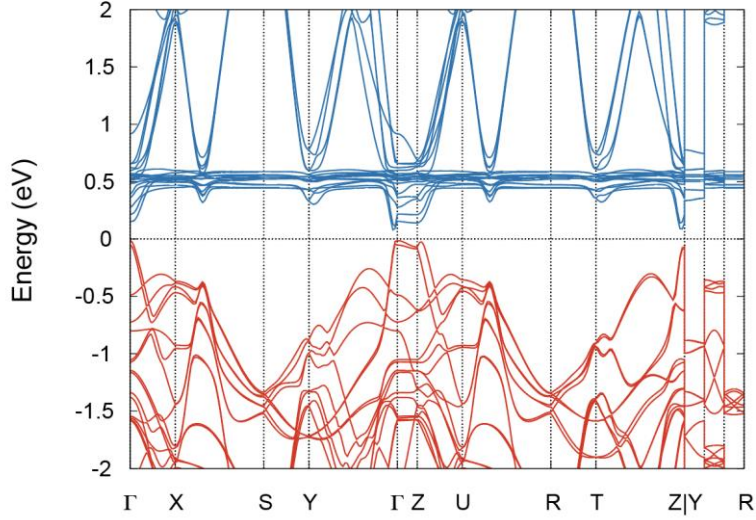


Figure S7. The calculated electronic band structure of collinear AFM ErAsS.

The band structure of collinear AFM ErAsS is shown in Fig. S7, from which we can see a global gap along the high-symmetry lines. All bands are two-fold degenerated in the collinear AFM state, thus Weyl nodes would not appear in this phase. Unlike the Kramer pairs protected by \mathcal{J} and \mathcal{T} , the parity eigenvalues are not necessary the same in the two degenerated states protected by \mathcal{J} and $\mathcal{T}\{\frac{1}{2}00\}$. In fact, on the $k_x = 0$ plane, the two degenerated states have the same parity. Whereas on the $k_x = \pi$ plane, they preserve different inversion eigenvalues for the additional a -directed fractional translation followed with time-reversal operator. Therefore, a Z_2 indicator on the plane $k_x = 0$ is defined with the AFM topological insulator. In the calculation, this Z_2 indicator should be zero. Besides, we checked the results by using the magnetic topological quantum chemistry (MTQC) theory [6, 7], the occupied band structure can be decomposed by the elementary band representation in magnetic space group, which also means it's a trivial insulator in the view of MTQC theory.

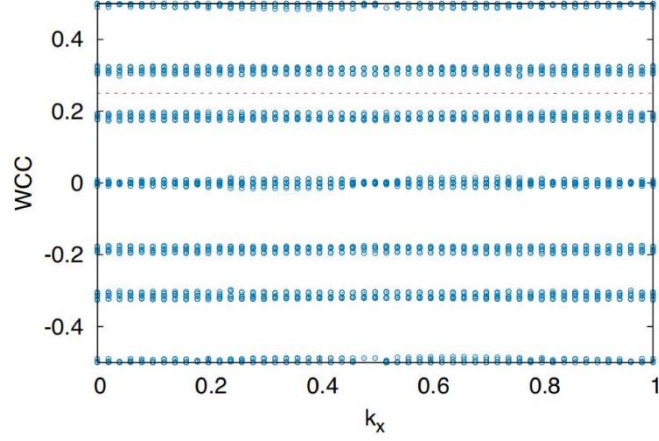


Figure S8. The Wilson loop spectrum for subspace with $+i$ mirror eigenvalue on $k_y = 0$ plane.

Table S5. The correspondence relation between topological invariants and symmetry indicators for magnetic space group 11.55.

Z_2	weak	$\{1 \frac{1}{2}00\}^*$	$Z_{\frac{1}{2}0}^{010}$	i	$Cm_{(2)}^{010}$
1	(000)	1	0	1	$1\bar{1}00$
0	(000)	0	0	0	$2\bar{2}00$

From Peng et al.'s work [8], we know that even the symmetry indicator is zero (Table S5) for magnetic space group 11.55, the mirror Chern number on $k_y = 0$ plane can still be nontrivial. (Noted that the mirror Chern number on $k_y = \pi$ plane must be zero). For such a reason, we calculated the Wilson loop spectrum on $k_y = 0$ plane for the subspace with $+i$ mirror eigenvalue (Fig. S8), and found that the mirror Chern number is also zero.

5. Experimental electronic structures

5.1 Angle-resolved photoemission spectroscopy measurements

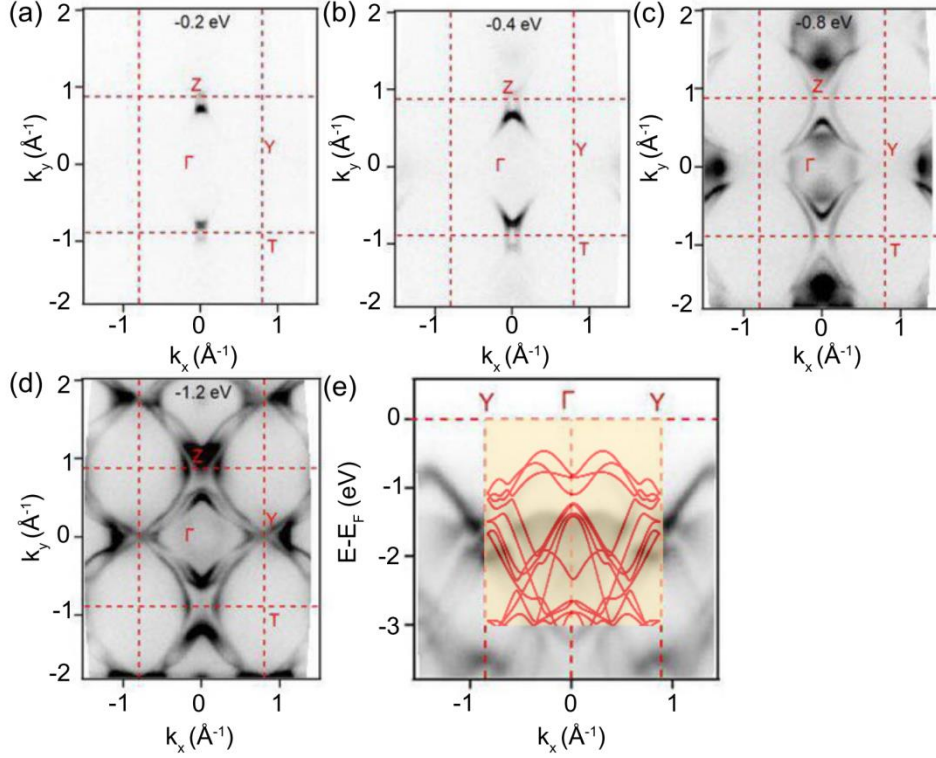


Figure S9. Constant energy contours at various binding energies (E_B) in the $k_x \sim k_y$ reciprocal plane. (a) $E_B = -0.2$ eV, (b) $E_B = -0.4$ eV, (c) $E_B = -0.8$ eV, and (d) $E_B = -1.2$ eV. (e) The experimental and calculated band structure along $Y - \Gamma - Y$. The red solid lines show the calculated results.

5.2 Scanning tunneling microscopy/spectroscopy (STM/STS)

The sample was cleaved along the (100) plane in the STM chamber and tested *in situ*. The STM image and STS were taken at 5 K using a chemical etched W tip, and the bias voltages were defined as the tip bias with respect to the sample. The zero bias voltage corresponds to the Fermi energy.

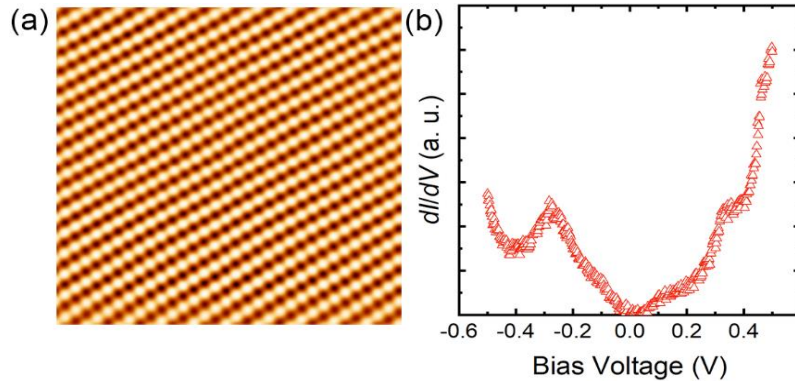


Figure S10. (a) STM image in a size of $10 \text{ nm} \times 10 \text{ nm}$. (b) STS in the bias voltage range of $-0.5 \text{ V} \sim 0.5 \text{ V}$.

- [1] G. M. Sheldrick, *Acta Crystallogr. Sect. A*, **2008**, *64*, 112-122.
- [2] O. V. Dolomanov, L. J. Bourhis, R. J. Gildea, J. A. K. Howard, H. Puschmann, *J. Appl. Crystallogr.*, **2009**, *42*, 339-341.
- [3] K. Shiozaki, M. Sato, K. Gomi, *Phys. Rev. B*, **2016**, *93*, 195413.
- [4] B. J. Wieder, B. Bradly, Z. J. Wang, J. Cano, Y. Kim, H. S. D. Kim, A. M. Rappe, C. L. Kane, B. A. Bernevig, *Science*, **2018**, *361*, 246-251.
- [5] A. Alexandradinata, Z. J. Wang, B. A. Bernevig, M. Zaletel, *Phys. Rev. B*, **2020**, *101*, 235166.
- [6] Y. F. Xu, L. Elcoro, Z. D. Song, B. J. Weider, M. G. Vergniory, N. Regnault, Y. L. Chen, C. Felser, B. A. Bernevig, *Nature*, **2020**, *586*, 702-707.
- [7] L. Elcoro, B. J. Weider, Z. D. Song, Y. F. Xu, B. Bradlyn, B. A. Bernevig, *Nat. Commun.* **2021**, *12*, 5965.
- [8] B. R. Peng, Y. Jiang, Z. Fang, H. M. Weng, C. Fang, (*Preprint*) *arXiv:2102.12645*, 10.48550/arXiv.2102.12645, **2021**.